Electronic structure, Curie temperature, and magnetic transport of a two-dimensional multiferroic $MnSe_2/In_2Se_3$ heterostructure

Zi-Wen Zhang,[1] Yu-Fei Lang,[1] Hui-Ping Zhu,[2] Bo Li,[2] Yu-Qing Zhao,[1,3,*] Bin Wei,[3,†] and Wu-Xing Zhou[1,4,‡]

[1] *School of Physics and Electronics Science, Hunan University of Science and Technology, Hunan Provincial Key Laboratory of Intelligent Sensors and New Sensor Materials, Xiangtan 411201, Hunan, People's Republic of China*

[2] *Institute of Microelectronics, Key Laboratory of Science and Technology on Silicon Devices, Chinese Academy of Sciences, Beijing 100029, China*

[3] *SKLSM, Institute of Semiconductors,Chinese Academy of Sciences, Beijing 100083, China*

[4] *School of Materials Science and Engineering, Hunan University of Science and Technology, Xiangtan 411201, People's Republic of China*

(Received 20 September 2023; revised 9 March 2024; accepted 29 April 2024; published 6 June 2024)

The coupling of ferromagnetic and ferroelectric materials has sparked great interest in the field of spintronics due to nonvolatile electrical magnetic control. In this work, we propose two-dimensional multiferroic $MnSe_2/In_2Se_3$ van der Waals (vdW) heterostructure to investigate the magnetoelectric coupling. The electronic structure, magnetic anisotropy, magnetic phase transition, and transport properties were investigated by employing the first-principles calculations in combination with the nonequilibrium Green's function method. The results reveal that polarization reversal not only can effectively tune the Schottky-to-Ohmic contact but also reorients the magnetic easy axis. In addition, Curie temperature (T_c) was predicted based on the Heisenberg model and Monte Carlo simulations, and the competition between interfacial charge injection and lattice mismatch determines the T_c of $MnSe_2/In_2Se_3$ heterostructure. Furthermore, we constructed the vdW $MnSe_2/In_2Se_3$-based magnetic-tunnel-junction and ferroelectric-tunnel-junction nanodevice, which exhibits high tunneling magnetoresistance of up to 1.805×10^3% and a spin-filter efficiency of up to 98.5%. Our findings demonstrate the significant potentials of multiferroic $MnSe_2/In_2Se_3$ vdW heterostructures in designing a next-generation spintronic and nonvolatile memory device.

DOI: 10.1103/PhysRevApplied.21.064012

I. INTRODUCTION

Nowadays, multiferroic materials have aroused great interest due to the co-existence of ferromagnetic (FM) and ferroelectric (FE) degrees of freedom [1–7]. The coupling of ferroelectricity and ferromagnetism facilitates the control of magnetism through electric field, and this magnetoelectric coupling effect plays a crucial role in the application of multifunctional devices. Since ferroelectricity requires unoccupied *d* orbitals, and ferromagnetism is generated by the occupation of partial *d* orbitals of transition metal atoms, which makes the two contradict each other, resulting in the scarcity of single-phase multiferroic materials in nature. This is also known as the d^0 rule in multiferroics [8–11]. As a consequence, most multiferroic designing strategy has focused on composite systems composed of alternating FM and FE materials at present [12–15].

In recent decades, a large amount of two-dimensional (2D) intrinsic van der Waals (vdW) magnets and ferroelectrics have been synthesized, such as $CrGeTe_3$ [16,17], CrI_3 [18,19], $MnBi_2Te_4$ [20,21], In_2Se_3 [22–24], and Sc_2CO_2 [25]. The above synthesized 2D magnets and ferroelectrics provide an enriched platform for designing alternative multiferroic building blocks. However, the above synthesized 2D ferromagnetic semiconductors exhibit a relatively low T_c, for example, for CrI_3 and $MnBi_2Te_4$, the T_c are only 45 [26] and 20 K [27], respectively, significantly below room temperature, thus hindering its commercial development and application. The recently discovered and synthesized $MnSe_2$ [28] by O'Hara *et al.* [29], qualifies as a room-temperature FM system, demonstrating its potential utility in nanoscale spintronic devices, such as sensors and memories [30,31]. However, under certain extreme conditions, room-temperature spintronic devices may not function properly.

*Corresponding author: yqzhao@hnu.edu.cn
†Corresponding author: binwei@semi.ac.cn
‡Corresponding author: wuxingzhou@hnu.edu.cn

Therefore, enhancing the T_c is one of the urgent issues that needs to be addressed at present. The general and convenient strategies to regulate the T_c as well as electronic, magnetic properties include vacancies [32], strain [33], and adsorption [34], which may be generated from the construction of 2D devices [35–38]. For example, the stress caused by lattice stretching or compression during epitaxial growth commonly leads to changes in electronic and magnetic properties, which is of great significance for practical applications and deserves our attention. On the other hand, a 2D FE semiconductor exhibits spontaneous polarization, and its polarization state can be regulated by an external electric field [39–44]. Due to the miniaturization and nonvolatility requirements of devices, ferroelectric tunnel junctions (FTJs) have been proposed and are considered to be one of the most promising memory types in the future. When 2D FE semiconductors with different polarization states are vertically stacked on 2D FM materials, it may lead to variations in the height and width of electron tunneling barriers, resulting in different charge transfers occurring at the interface [45,46]. Furthermore, the occupancy ratio of *d* orbital and electron concentration of 2D FM materials may change with different polarization states of 2D FE semiconductors, which can affect the magnetism [47,48]. Based on this, the concept of other electronic devices that are composed of 2D FM and FE materials are proposed, in which the FE barrier layer is sandwiched between two magnetic layers. The coexistence of FTJs and MTJs provides an enriched physical platform to investigate tunneling magnetoresistance (TMR) and tunneling electroresistance (TER), offering the possibility of discovering devices with excellent spin-transport performances.

In this work, we firstly stacked 2D monolayer FE In_2Se_3 semiconductor onto 2D monolayer FM $MnSe_2$ metal to construct the multiferroics vdW heterostructure. By using first-principles simulations, we found that the electrical contact and easy magnetization axis of heterostructures composed of $MnSe_2$ and In_2Se_3 are controlled by the polarization direction of In_2Se_3. The calculated T_c of pristine monolayer $MnSe_2$ based on the Heisenberg model is 296 K, which is in good agreement with the experimental results [49]. However, when stacking onto In_2Se_3, the T_c of $MnSe_2$ decreased to varying degrees whatever the polarization direction. The calculated charge-density difference reveals that the electrons transfer from In_2Se_3 to $MnSe_2$, favoring the T_c increase. However, compressed lattice strain cause the decrease of T_c in $MnSe_2$, and vice versa. The competition between charge injection and lattice strain ultimately determines the T_c of $MnSe_2/In_2Se_3$ heterostructures. Finally, the multiferroic $MnSe_2/In_2Se_3/MnSe_2$-based devices were constructed to utilize the magnetoelectric coupling to control the interface to investigate TMR, TER, and spin-transport properties, and remarkable TMR were obtained. These investigations provide a basis for the design of nonvolatile micro- and nanomemory devices in the future.

II. CALCULATION METHOD

Density-functional-theory (DFT) calculations were carried out using the Vienna *ab initio* simulation package (VASP) and the electron correlation and exchange interaction are described by the Perdew-Burke-Ernzerhof (PBE) functional [50–54]. The energy cutoff was set to be 500 eV for the plane-wave expansion with a $9 \times 9 \times 1$ and $4 \times 4 \times 1$ k-point meshes for $MnSe_2$ and $MnSe_2/In_2Se_3$, respectively. All atoms are allowed to be fully relaxed till the atomic Hellmann-Feynman forces are less than 0.001 eV/Å. The convergence criterion of energy in the self-consistency process is set to be 1×10^{-7} eV. In order to describe the on-site Coulomb repulsion between the localized electrons, the effective onsite Coulomb interaction parameter (U) is set as $U = 3.9$ eV [55] and Hund's coupling (J) is set as $J = 0$ eV for Mn. The spin-orbit coupling (SOC) is considered in band simulation. The vdW interaction is taken into consideration by employing the DFT-D3 functional [56]. In addition, a large vacuum thickness of 15 Å along the z axis was set to avoid interaction between periodical slabs.

The quantum transport calculations were performed by using the nonequilibrium Green's function-density functional theory (NEGF DFT) method implemented in the NanoDCAL package [57,58]. The linear combination atomic orbital (LCAO) method with the double-ζ polarized (DZP) functions was adopted for the microelectronic device calculations. For the $Cu/MnSe_2/In_2Se_3/MnSe_2/Cu$ device, the cutoff was set as 80 hartree and the electron temperature was set at 100 K. In the self-consistent calculations, a $9 \times 9 \times 2$ k-point meshes was used to calculate the Hamiltonian matrix and density matrix and the convergence criterion of energy was set to be 1×10^{-4} eV. On the basis of self-consistency, a $100 \times 100 \times 1$ k-point meshes was adopted to calculate the I-V characteristics. The spin-polarization current under bias can be calculated using the Landauer-Büttiker formula [59], as follows:

$$I_\sigma(V_{\text{bias}}) = \frac{e}{h}\int \{T_\sigma(E, V_{\text{bias}})[f_L(E, V_{\text{bias}}) - f_R(E, V_{\text{bias}})]\}\, dE, \quad (1)$$

where $T_\sigma(E, V_{\text{bias}})$ is the spin-polarized transmission probability, $f_{L/R}(E, V_{\text{bias}})$ is the Fermi–Dirac distribution function of the left (L) or right (R) electrode, and σ represents spin freedom.

III. RESULTS AND DISCUSSION

A. Geometrical structure and binding energy

Figure 1(a) shows the side view of atomic structures of

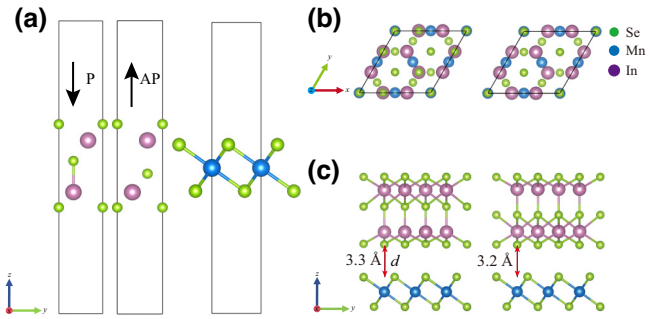

FIG. 1. (a) The side view of In_2Se_3-P (left), In_2Se_3-AP (middle), and $MnSe_2$ (right). (b) The top and (c) side view of optimized atomic geometric structures of $MnSe_2/In_2Se_3$-P (left) and $MnSe_2/In_2Se_3$-AP (right).

free-standing monolayer α-In_2Se_3 and 1T-$MnSe_2$. The left and middle panel are In_2Se_3-P and In_2Se_3-AP, where P and AP represent two opposite ferroelectric polarization state. The right panel is monolayer $MnSe_2$. The α-In_2Se_3 and 1T-$MnSe_2$ belong to the $R3m$ and $P3m1$ space groups with hexagonal symmetry. The in-plane lattice constants $a = b$ are 4.11 and 3.64 Å for α-In_2Se_3 and 1T-$MnSe_2$, respectively. The α-In_2Se_3 possesses room-temperature out-of-plane ferroelectricity down to monolayer while monolayer 1T-$MnSe_2$ exhibits ferromagnetic behavior with out-of-plane magnetization. Thus, 2×2 supercell 1T-$MnSe_2$ can be stacked onto $\sqrt{3} \times \sqrt{3}In_2Se_3$ to construct $MnSe_2/In_2Se_3$-P and $MnSe_2/In_2Se_3$-AP heterostructures, as shown in Figs. 1(b) and 1(c), where green, blue, and purple balls indicate Se, Mn, and In atoms, respectively. The optimized in-plane lattice $a = b$ for $MnSe_2/In_2Se_3$-P and $MnSe_2/In_2Se_3$-AP heterostructures are 7.12 and 7.14 Å, respectively, along with small lattice mismatch 0.62%. The lattice mismatch is lower than 5%, thus fulfilling the requirements for heterostructure epitaxial growth in experiments. The symbol d, indicated by the red arrow in Fig. 1(c), signifies the optimized equilibrium distance between the $MnSe_2$ and In_2Se_3 slab. Table S1 and Fig. S1 within the Supplemental Material [60] demonstrate the equilibrium distance for $MnSe_2/In_2Se_3$-P and $MnSe_2/In_2Se_3$-AP heterostructures are 3.3 and 3.2 Å, respectively. To evaluate the stability of the $MnSe_2/In_2Se_3$ heterostructure, the binding energies E_b were calculated and defined as

$$E_b = E_{\text{heter}} - E_{MnSe_2} - E_{In_2Se_3}, \tag{2}$$

where E_{heter} is the total energy of the heterostructure, E_{MnSe_2} and $E_{In_2Se_3}$ are the total energy of the free-standing monolayer $MnSe_2$ and In_2Se_3, respectively. The calculated binding energies E_b of $MnSe_2/In_2Se_3$-P and $MnSe_2/In_2Se_3$-AP heterostructures are -3.19 and -3.25 eV, respectively, listed in Table S1 within the Supplemental Material [60], and negative value E_b benefits from the formation of the $MnSe_2/In_2Se_3$ heterostructure. Therefore, the heterostructures vertically stacked by $MnSe_2$ and In_2Se_3 are stable.

B. Magnetic anisotropy and electronic structure

Magnetic anisotropic energy (MAE) refers to the energy difference along with magnetization is oriented in different directions, and is defined as $\text{MAE} = (E_{uvw} - E_{\text{min}})/n$, where E_{uvw} and E_{min} denote the total energy in any magnetization direction and along the most stable magnetization direction, respectively. n represents the number of Mn atoms. Figures 2(a)–2(c) show the polar angle dependence of MAE in the x-y and x-z planes. The calculated results reveal the magnetization easy axis of the free-standing monolayer $MnSe_2$ is out of plane, which is consistent with previous results, as shown in Fig. 2(a). The equal magnetic energy of all directions in the x-y plane indicates that $MnSe_2$ is magnetic isotropic in plane. The magnetization easy axis deviates in (001) direction by 30° in $MnSe_2/In_2Se_3$-P while the magnetization easy axis in the $MnSe_2/In_2Se_3$-AP heterostructure still remains in the (001) direction, as shown in Figs. 2(b) and 2(c). Based on the calculated magnetization easy axis, band structures of $MnSe_2/In_2Se_3$-P and $MnSe_2/In_2Se_3$-AP heterostructures were calculated with inclusion SOC effects, and the results show that the conduction-band minimum (CBM) and valence-band maximum (VBM) locate in the high symmetric point Γ in the first Brillouin zones (FBZs) with direct band gap, as shown in Figs. 2(d) and 2(e). Thus, the extracted band gap from Figs. 2(d) and 2(e) are 0.91 and 0.80 eV, respectively. Further investigation reveals the $MnSe_2/In_2Se_3$-P heterostructure belongs to p-type Schottky contact as the Fermi level (E_F) crosses the gap, and is close to the VBM. The $MnSe_2/In_2Se_3$-AP heterostructure belongs to n-type Ohmic contact as the E_F is shallower than the CBM. For the Schottky-Ohmic contact transition, spontaneous polarization generates positive and negative bound charges, and the interface polarization electric field generated by the bound charges is in the same or opposite direction to the built-in electric field generated by the metal-semiconductor contact, leading to a change in contact type [61]. Refer to Figs. S8 and S9 within the Supplemental Material [60] for details.

C. Magnetic exchange interactions, phase diagram, and magnetic mechanism

Ideal T_c is one of the decisive factors to determine whether 2D magnetic materials can be applied in spintronics at room temperature. For the material we are exploring, its magnetic phase diagram and magnetic transition temperature T_c from FM to paramagnetic state can be characterized by the XXZ Heisenberg Hamiltonian model based on the Monte Carlo (MC) method [62]. The spin

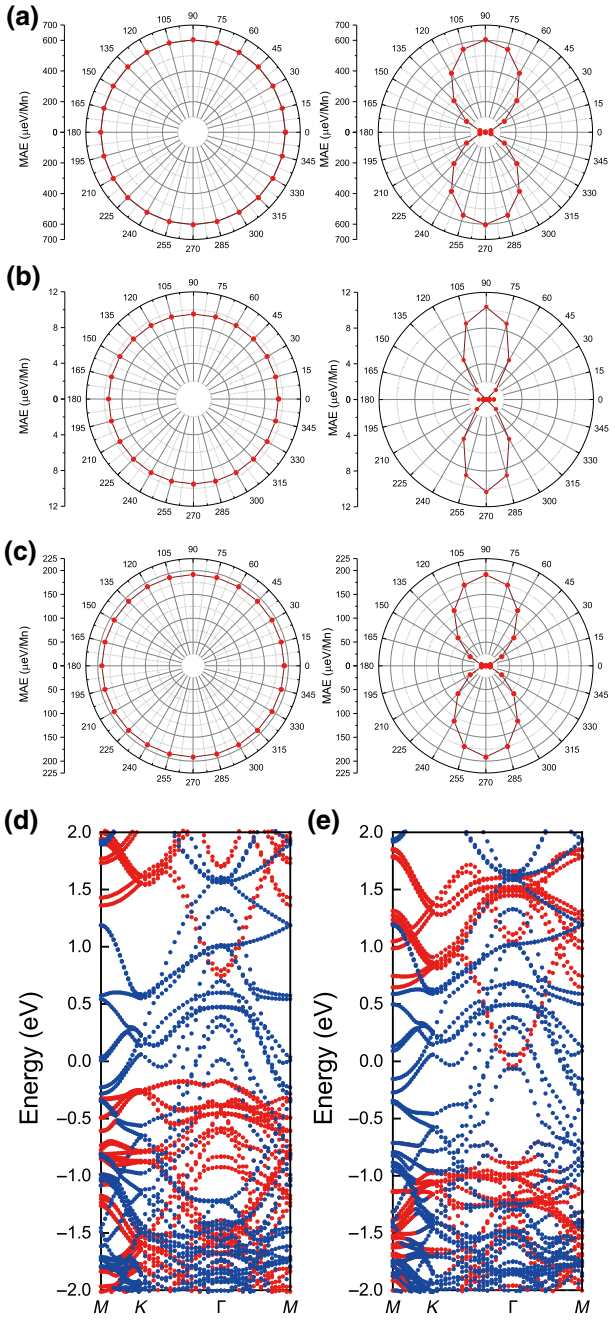

FIG. 2. The MAE of (a) free-standing monolayer $MnSe_2$, (b) $MnSe_2/In_2Se_3$-P, and (c) $MnSe_2/In_2Se_3$-AP heterostructures in the x-y (left) and x-z (right) plane, where 0° in the x-z plane represents the 001 direction. Projected band structures of (d) $MnSe_2/In_2Se_3$-P and (e) $MnSe_2/In_2Se_3$-AP heterostructures. The blue and red lines represent the electronic orbital contributions of $MnSe_2$ and In_2Se_3, respectively.

Hamiltonian is defined as

$$H = -\left(J\sum_{i,j}\vec{S}_i\cdot\vec{S}_j + \lambda\sum_{i,j}S_i^zS_j^z + D\sum_i(S_i^z)^2\right), \quad (3)$$

where S_i represents the spin vector of the i th Mn atom. J and λ denote the nearest-neighbor (NN) isotropy and anisotropy exchange interaction, respectively. D is easy-axis, single-ion anisotropy. Here, the second NN and farther interaction are neglected due to a smaller order of magnitude. The values of J, λ, D can be obtained by constructing different magnetic configurations labeled as FM,z, FM,x, AFM,z, and AFM,x, as shown in Fig. S2 within the Supplemental Material [60]. Thus, the magnetic configuration total energies associated with J, λ, D can be written as

$$H_{\mathrm{FM},z} = -48J - 48\lambda - 16D + H_0, \quad (4a)$$

$$H_{\mathrm{FM},x} = +16J + 16\lambda - 16D + H_0, \quad (4b)$$

$$H_{\mathrm{AFM},z} = -48J + H_0, \quad (4c)$$

$$H_{\mathrm{AFM},x} = +16J + H_0, \quad (4d)$$

where H are total energies in different magnetic configuration while H_0 are nonmagnetic energies. The calculated J, λ, and D are 6.266, 0.029, and −0.020 meV, listed in Table I. We adopted the finite-size $L\times L\times 1$ supercell ($[L=16, L=180]$) to reperform MC simulations with the Metropolis algorithm to investigate magnetic phase transition, in which 80 000 sweeps were performed to achieve the thermal equilibrium for each temperature, and all data including magnetic moment and specific heat capacity are extracted from 840 000 sweeps. Figures 3(a)–3(c) plot the normalized magnetization and specific heat as the function of temperature with $L=64$ lattices for for $MnSe_2$, $MnSe_2/In_2Se_3$-P, and $MnSe_2/In_2Se_3$-AP heterostructures. The normalized magnetization in Fig. 3(a) indicated by the red dotted line decreases with temperature and drops sharply at around 310 K and the specific heat capacity indicated by blue dotted line reaches a peak at this temperature. Thus, the calculated 310 K with $L=64$ lattices is the ferromagnetic-paramagnetic phase transition T_c for free-standing $MnSe_2$ in Fig. 3(a). The inserts of the figures demonstrate Curie temperature versus inverse finite lattice size $1/L$ with ($[L=16, L=96]$). The intersection point of the linearly fitted dotted line and the temperature axis represents the accurate MC result ($T_c=296$ K) of infinite-scale lattice $L\to\infty$, as the lattices of 2D magnets in experiments are infinitely extended in the plane. Thus, the calculated T_c approximately 296 K of free-standing $MnSe_2$

TABLE I. The nearest-neighbor isotropy exchange interaction (J), anisotropy exchange interaction (λ), single-ion anisotropy (D), and T_c of $MnSe_2$, $MnSe_2/In_2Se_3$-P, and $MnSe_2/In_2Se_3$-AP.

System	J (meV)	λ (meV)	D (meV)	T_c (K)
$MnSe_2$	6.266	0.029	−0.020	296
$MnSe_2/In_2Se_3$-P	4.922	0.079	−0.244	243
$MnSe_2/In_2Se_3$-AP	5.561	0.101	−0.254	278

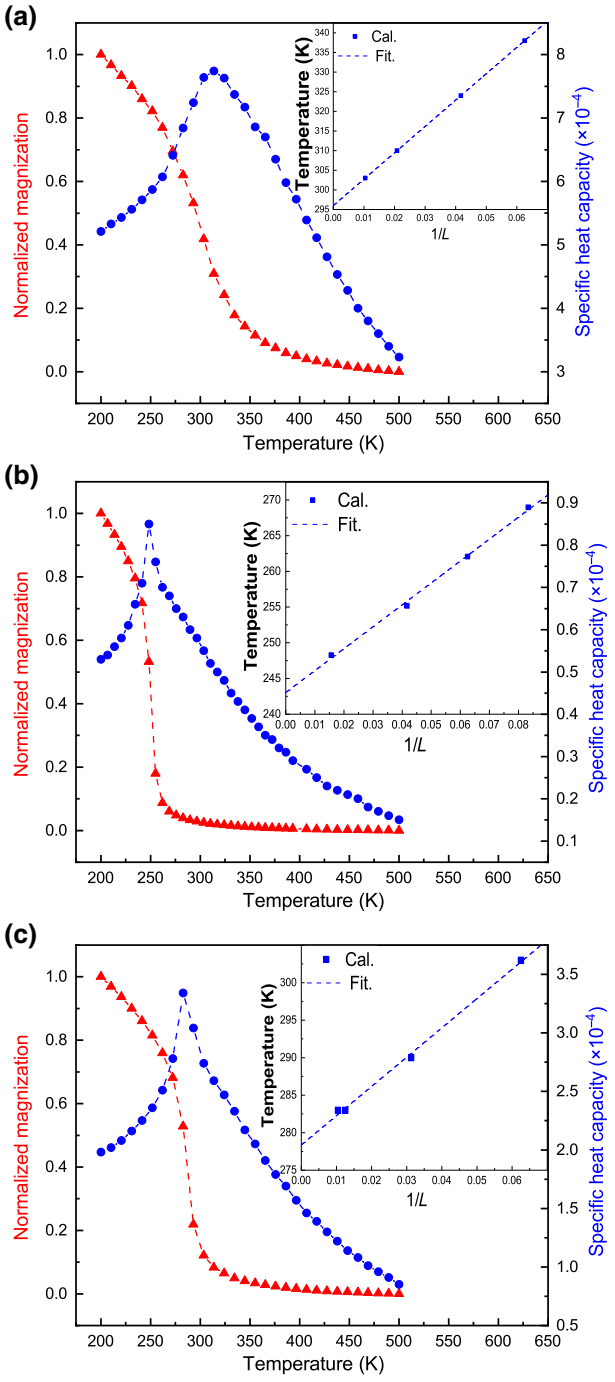

FIG. 3. The normalized magnetization (red dots) and specific heat capacity (blue triangles) as functions of temperature for (a) monolayer $MnSe_2$, (b) $MnSe_2/In_2Se_3$-P, and (c) $MnSe_2/In_2Se_3$-AP. The inserts depict the transition temperatures T_c as functions of $1/L$.

is in good accordance with the experiments approximately 300 K [42]. Similarly, Figs. 3(b) and 3(c) demonstrate T_c of $MnSe_2/In_2Se_3$-P and $MnSe_2/In_2Se_3$-AP heterostructures are 243 and 278 K when $L \to \infty$, respectively.

To identify the magnetic exchange mechanism of $MnSe_2/In_2Se_3$ heterostructures, we firstly plotted the projected density of states (PDOS) of $d_{x^2-y^2}$, d_{xy}, d_{xz}, d_{yz}, and d_{z^2} orbitals of free-standing $MnSe_2$, as shown in Fig. 4(a). All spin-up channels of d orbitals indicated by black lines are occupied while spin-down channels are almost empty. The above results suggest theoretical magnetic moment should have been 5 μB per Mn, however it is higher than calculated magnetic moment 4 μB per Mn [63]. It should be noted that a few partial spin-down channel of $d_{x^2-y^2}$, d_{xy}, d_{xz}, d_{yz} are also partially occupied at the energy of −2 eV, owing to the spin transfer between the Mn-Se covalent bond, thus canceling out a few magnetic moments according to Hund's rule. All d orbitals split into $d_{x^2-y^2}/d_{xy}$, d_{xz}/d_{yz}, and d_{z^2}, in which generated $d_{x^2-y^2}/d_{xy}$ orbitals occupy the highest spin-up energy levels, and the d_{z^2} orbitals occupy the lowest spin-up energy level. Figure S3 within the Supplemental Material [60] demonstrates the PDOS of $MnSe_2/In_2Se_3$-P and $MnSe_2/In_2Se_3$-AP heterostructures, and the occupied states of spin are nearly similar to free-standing $MnSe_2$, thus being the FM state, in accordance with the NN exchange interaction J. Figure 4(b) is the direct and superexchange of the schematic diagram between the NN Mn atoms. Based on the general band-coupling model [64–66], the direct exchange interactions between the half-occupied d-orbital overlaps of the NN Mn atoms favor AFM coupling. However, the direct AFM exchanges are weak due to the large Mn-Mn distance 3.49, 3.60, 3.55 Å for free-standing $MnSe_2$, $MnSe_2/In_2Se_3$-P, $MnSe_2/In_2Se_3$-AP heterostructures, as shown in Fig. 4(c). Moreover, the superexchange Mn1-Se-Mn2 angles in our models are about 89.8°, 90.47°, 88.66° for free-standing $MnSe_2$, $MnSe_2/In_2Se_3$-P, $MnSe_2/In_2Se_3$-AP heterostructures, respectively, listed in Table S1 within the Supplemental Material [60]. According to the Goodenough-Kanamori-Anderson (GKA) rules [67,68], 90° superexchange favors FM coupling, and 180° superexchange favors AFM coupling. Thus, all near-90° superexchanges Mn1-Se-Mn2 favor FM states, and Fig. 4(d) illustrates the one superexchange channel via the near-90° Mn($d_{x^2-y^2}$)-Se(p_x,p_y)-Mn($d_{x^2-y^2}$) bonds as example. The competitive relationship between direct exchange and superexchange determines the NN exchange. Table I demonstrates the NN exchanges J in both heterostructures decrease, thus causing the T_c to decrease down to 243 and 278 K for $MnSe_2/In_2Se_3$-P and $MnSe_2/In_2Se_3$-AP, respectively. In order to explain the above phenomenon, The planar-averaged differential charge were calculated, as shown in Figs. 5(a) and 5(b), where the red and blue regions represent charge depletion and accumulation, respectively. Figure 5(a) qualitatively demonstrates electrons transfer from In_2Se_3 to $MnSe_2$ at the interface of $MnSe_2/In_2Se_3$-P heterostructure while electron transfers of $MnSe_2/In_2Se_3$-AP heterostructure are ambiguous in Fig. 5(b). Therefore, quantitative Bader charges were further calculated, the analysis reveals charge transfer of 0.051e and 0.010e

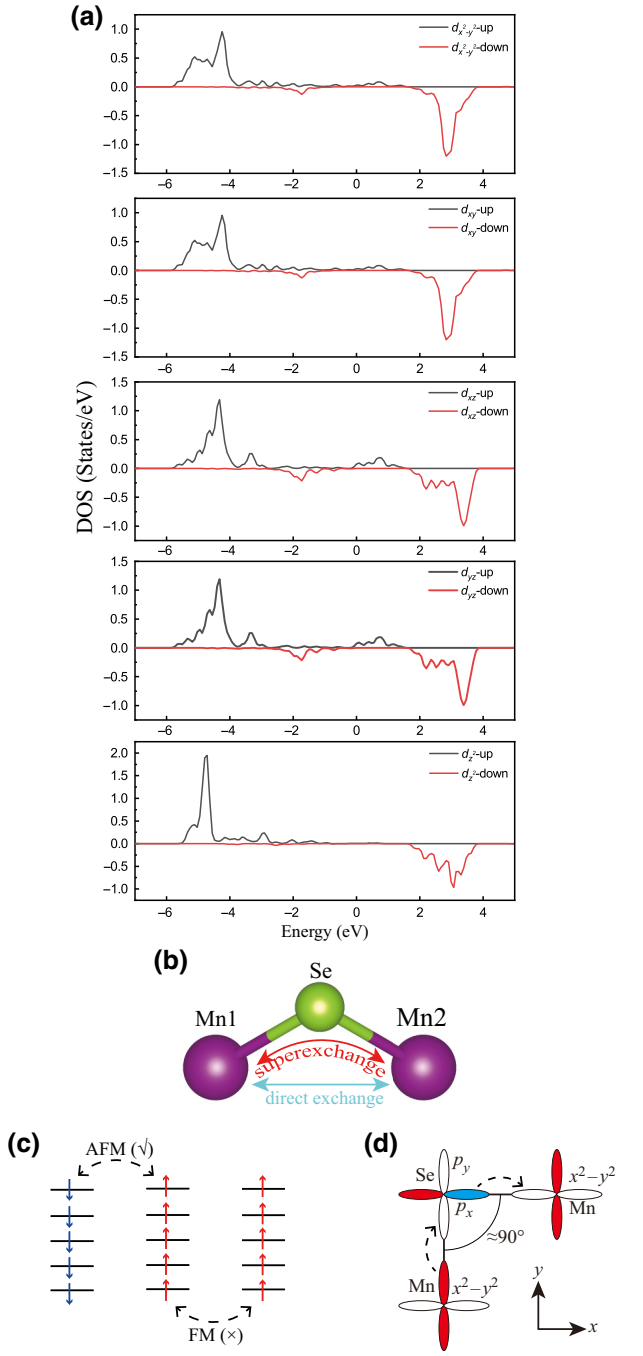

FIG. 4. (a) The projected density of states of $d_{x^2-y^2}$, d_{xy}, d_{xz}, d_{yz}, and d_{z^2} orbitals for Mn atoms in the intrinsic $MnSe_2$. (b) The description of the direct exchange and superexchange interaction between Mn atoms. (c) Sketch illustrating hopping processes in the two half-filled Mn d-orbital case of a direct overlap. (d) FM superexchange between two half-filled Mn d orbitals via Se p orbitals.

from In_2Se_3 to $MnSe_2$ for both heterostructures, indicating electrons move into $MnSe_2$ whatever the ferroelectric polarization states. However, the T_c of monolayer $MnSe_2$ increases in the case of doping electron [69], which is not in accordance with our calculated trend of T_c in

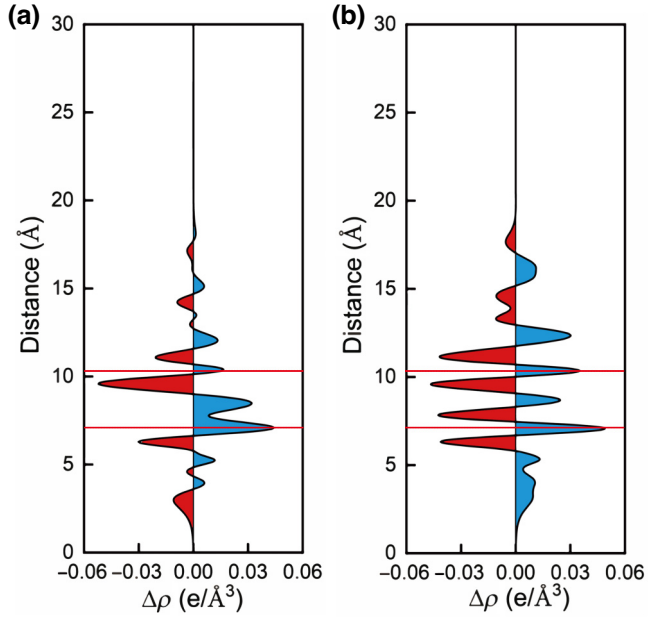

FIG. 5. The planar-averaged differential charge density of (a) $MnSe_2/In_2Se_3$-P and (b) $MnSe_2/In_2Se_3$-AP. The red and blue regions represent charge depletion and accumulation, respectively.

$MnSe_2/In_2Se_3$ heterostructures. We speculated the discrepancy may be ascribed to the lattice mismatch strain between the $MnSe_2$ and In_2Se_3 interface.

To verify the effects of lattice mismatch on J, we firstly applied biaxial in-plane compressing and stretching strain to the lattice of free-standing monolayer $MnSe_2$ increasing from -0.03 to 0.03, as shown in Fig. 6. The green, black, and red dot lines represent the J of free-standing $MnSe_2$, $MnSe_2/In_2Se_3$-P, and $MnSe_2/In_2Se_3$-AP heterostructures, respectively. The J of free-standing $MnSe_2$ and $MnSe_2/In_2Se_3$ heterostructures increase with the lattice strain varying from -0.03 to 0.03. The specific J, λ, D, and T_c are shown in Table S2–S4 and Fig. S4 within the Supplemental Material [60]. Additionally, the results of T_c under 0.03 compressive stresses by the MC methods are shown in Fig. S5 within the Supplemental Material [60]. The optimized lattice a, b of 2×2 supercell $MnSe_2$, $MnSe_2/In_2Se_3$-P, and $MnSe_2/In_2Se_3$-AP were calculated to be 7.24, 7.12, and 7.14 Å, listed in Table S1 within the Supplemental Material [60]. Obviously, the lattice of $MnSe_2$ in the heterostructures are all compressed compared with free-standing 2×2 supercell $MnSe_2$. Combining our above calculations, lattice compression dominates in the competition between lattice compression and charge injection, which leads to a decrease in the J of $MnSe_2/In_2Se_3$ heteroostructures. In actual experiments, we can utilize the epitaxial growth method to suppress compressive stress and enhance the T_c in $MnSe_2/In_2Se_3$ heterostructures.

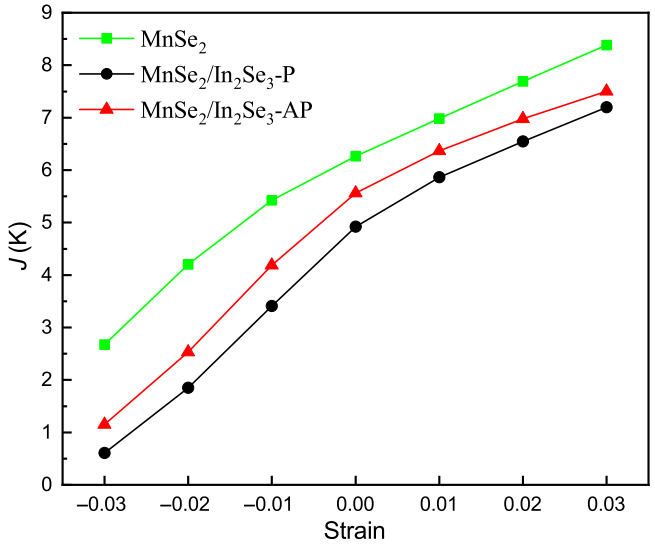

FIG. 6. The nearest-neighbor isotropy exchange interaction J as a function of applying biaxial compressing and stretching strain, varying from −0.03 to 0.03 with the minimum interval of 0.01.

D. Tunneling magnetoresistance, electroresistance and spin filter on $MnSe_2/In_2Se_3/MnSe_2$ MFTJs

The two spontaneous polarization states of P and AP in ferroelectric In_2Se_3 can be reversibly switched by applying an external electric field while the $MnSe_2$ is magnetic. The characteristics of magnetoelectric coupling are often utilized to design memory device. Here we construct the two-probe nanodevice $Cu/MnSe_2/In_2Se_3$-P(AP)/$MnSe_2$/Cu MFTJs to unveil how the huge contrasting behaviors in the coupling of polarization states P(AP) of the monolayer In_2Se_3 and magnetic states FM (AFM) of bilayer $MnSe_2$ can be utilized for valving applications. The $MnSe_2/In_2Se_3$-P(AP)/$MnSe_2$ are the central scattering region and the Cu(111) slab is the electrode, as shown in Figs. 7(a) and 7(b). The optimized distance between electrode Cu(111) slab and adjacent $MnSe_2$ are 3.0 Å. Figures 7(c)–7(f) demonstrate four ordered configurations of the nanodevice, labeled as P-FM, AP-FM, P-AFM, and AP-AFM. The left contact between $MnSe_2/In_2Se_3$ are Schottky and Ohmic contacts, and conversely the right contact are Ohmic and Schottky contacts in Figs. 7(c) and 7(d), respectively (detailed electronic calculation can be seen in Fig. S6 within the Supplemental Material [60]). Further, according to the Simmons model [70], the electron tunneling resistivity (ρ_t) can be defined as

$$\rho_t = \frac{4\pi^2\hbar d_{\mathrm{TB}}^2}{e^2} \frac{\exp\left[\frac{2}{\hbar}\left(2m_e^{\frac{1}{2}} d_{\mathrm{TB}}\phi_{\mathrm{TB}}^{\frac{1}{2}}\right)\right]}{\frac{(2m_e)^{\frac{1}{2}} d_{\mathrm{TB}}\phi_{\mathrm{TB}}^{\frac{1}{2}}}{\hbar} - 1}, \tag{5}$$

where $\hbar$ and m_e represent the reduced Planck constant and free electron mass. The d_{TB} and ϕ_{TB} represent the barrier width and height, respectively, and the corresponding value are listed in Table S5 within the Supplemental Material [60]. The calculated ρ_t and contact type are marked in Figs. 7(c) and 7(d). The P-FM, AP-FM, P-AFM, and AP-AFM-ordered configuration correspond to four total currents $I_{\text{P-FM}}$, $I_{\text{AP-FM}}$, $I_{\text{P-AFM}}$, $I_{\text{AP-AFM}}$, which are divided into spin-resolved currents $I_{\text{P-FM}(\uparrow)}$, $I_{\text{AP-FM}(\uparrow)}$, $I_{\text{P-AFM}(\uparrow)}$, $I_{\text{AP-AFM}(\uparrow)}$, $I_{\text{P-FM}(\downarrow)}$, $I_{\text{AP-FM}(\downarrow)}$, $I_{\text{P-AFM}(\downarrow)}$, $I_{\text{AP-AFM}(\downarrow)}$, as shown in Figs. 7(g) and 7(h). The total currents $I_{\text{AP-FM}}$ in the AP-FM-ordered configuration are larger than $I_{\text{P-FM}}$ of the P-FM-ordered configuration. The phenomenon can be attributed to the contact resistance, and the contact resistances of AP-FM-ordered configuration are 2.38×10^{-9} and 2.31×10^{-9} Ω cm^2, which are smaller than 2.98×10^{-9} and 2.68×10^{-9} Ω cm^2 in P-FM-ordered configuration for Ohmic and Schottky contacts. Moreover, both total currents $I_{\text{AP-FM}}$ and $I_{\text{P-FM}}$ are one magnitude larger than total currents $I_{\text{AP-AFM}}$ and $I_{\text{P-AFM}}$ when the $MnSe_2$ layers transform from FM-ordered into AFM-ordered configuration, due to the TMR effect. Also, as the bias voltage increases from 0 to 0.1 V, the spin-resolved currents keep increasing. However, the spin-up currents $I_{\text{P-FM}(\uparrow)}$, $I_{\text{AP-FM}(\uparrow)}$ are much larger than spin-down currents $I_{\text{P-FM}(\downarrow)}$, $I_{\text{AP-FM}(\downarrow)}$ in all FM-ordered configuration while the spin-down currents $I_{\text{P-AFM}(\uparrow)}$, $I_{\text{AP-AFM}(\uparrow)}$ are slightly larger than $I_{\text{P-AFM}(\downarrow)}$, $I_{\text{AP-AFM}(\downarrow)}$ in all AFM-ordered configuration. Based on the calculated total and spin-resolved currents, thereby TMR, TER and SFE(η) can be evaluated and defined as

$$\mathrm{TMR} = \frac{I_{\mathrm{FM}} - I_{\mathrm{AFM}}}{I_{\mathrm{AFM}}}, \tag{6}$$

$$\mathrm{TER} = \frac{I_{\mathrm{AP}} - I_{\mathrm{P}}}{I_{\mathrm{P}}}, \tag{7}$$

$$\eta = \frac{I_{\uparrow} - I_{\downarrow}}{I_{\uparrow} + I_{\downarrow}}, \tag{8}$$

where I_{FM} and I_{AFM} represent the total current of FM- and AFM-ordered configuration, respectively. I_{P} and I_{AP} represent the total current of P- and AP-ordered configuration, respectively. $I_{\uparrow}$ and $I_{\downarrow}$ represent the spin-up and spin-down current of the all-ordered configuration.

Figure 7(i) displays the TMR and TER with increase of bias voltage. The TMR maintains about 1000% and 1740% for P-ordered and AP-ordered configuration, respectively, in which the maximum TMR reaches extremely high above 1800% at the bias voltage of 0.04 and 0.1 V. The difference between $I_{\text{AP-FM}}$ and $I_{\text{AP-AFM}}$ in AP-ordered configuration is larger than that in P-ordered configuration, thus of causing the larger tunneling magnetoresistance in AP-ordered configuration TMR-AP than TMR-P in P-ordered configuration. The TER is caused by

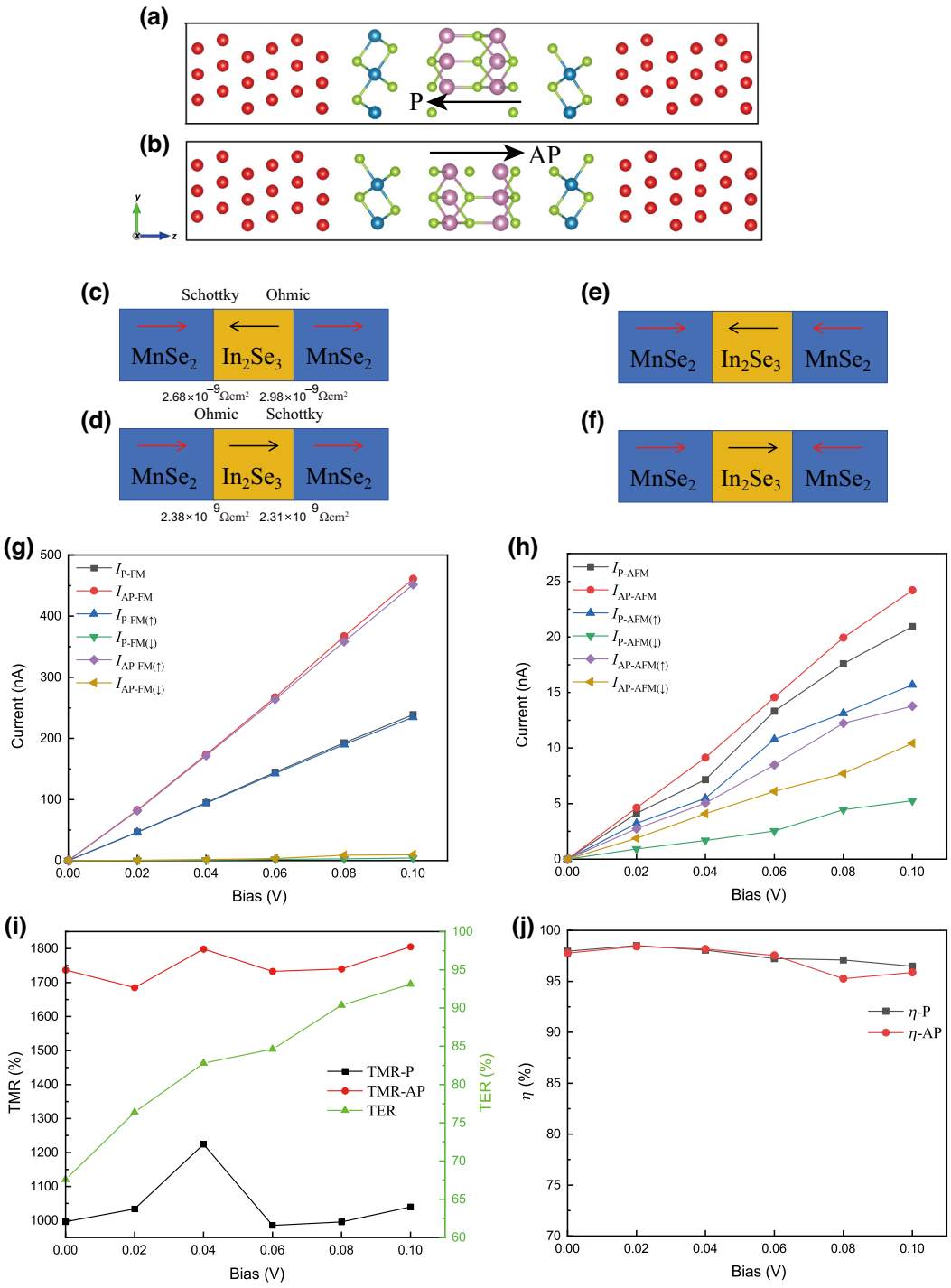

FIG. 7. The structures diagram of (a) $MnSe_2/In_2Se_3$-P/ $MnSe_2$ and (b) $MnSe_2/In_2Se_3$-AP/ $MnSe_2$ MFTJs, the black arrows P and AP represent the polarization direction of In_2Se_3. The (c) P-FM (d) AP-FM (e) P-AFM (f) AP-AFM-ordered configuration of the central scattering region. The currents in the (g) FM and (h) AFM-ordered configuration with respect to different finite bias voltage. The (i) TMR, TER and (j) SFE (η) of $MnSe_2/In_2Se_3/MnSe_2$ MFTJs.

the difference between I_P and I_{AP} when the ferroelectric state reversals. The TER indicated by the green triangle line in FM-ordered configuration increases with the increase of bias voltage from 0 to 0.1 V,and reaches up to maximum of 93%. Figure 7(j) demonstrates the SFE(η) slightly increases as the bias voltage increases from 0 to 0.02 V, then generally maintains a downward trend with the increase of bias voltage from 0.02 to 0.1 V in both P-FM-ordered and AP-FM-ordered configuration. The η keep above 95%, approaching perfect

spin filtering, which is consistent with the calculated spin band structures shown in Fig. S7 within the Supplemental Material [60]. The spin-up channels are largely occupied while most spin-down channels are empty near the E_F. The remarkable TMR and SFE reveal that $Cu/MnSe_2/In_2Se_3/MnSe_2/Cu$ MFTJs are potentially useful in nanoscale spintronics.

IV. CONCLUSIONS

To sum up, we systematically investigated the electronic, magnetic, and transport properties of the 2D multiferroic $MnSe_2/In_2Se_3$ heterostructures by employing first-principles and NEGF methods. The results reveal the Schottky-Ohmic contact and magnetic easy axis can be reversibly regulated by electrically switching the ferroelectric polarization of monolayer In_2Se_3. The T_c in 2D $MnSe_2/In_2Se_3$ heterostructures can be effectively tuned in the competition of biaxial stress and charge transfers. Furthermore, the quantum transport calculation of the proof-of-concept two-probe nanodevice based on both $MnSe_2/In_2Se_3$-P/ $MnSe_2$ and $MnSe_2/In_2Se_3$-AP/ $MnSe_2$ vdW heterostructures demonstrate a remarkable TMR, TER, and SFE with respect to the bias voltage, and the averaged TMR, TER, and SFE reach 1805%, 93% and 98.5%. The nonvolatile controls enrich the multifunctionalities in 2D multiferroic $MnSe_2/In_2Se_3$ heterostructures, and our findings demonstrate the significant potential applications of multiferroic $MnSe_2/In_2Se_3$ vdW heterostructures in designing next-generation spintronic and nonvolatile memory devices.

ACKNOWLEDGMENTS

This work was supported by the National Natural Science Foundation of China (NSFC) (Grants No. 12204166, No. 12205093, No. 12247115), the Scientific Research Fund of Hunan Provincial Education Department, China (Grant No. 20B219), Initial Scientific Research Fund of Hunan University of Science and Technology through Grant No. E51996, the Postgraduate Research Opportunities Program of HZWTECH (HZWTECH-PROP). We gratefully acknowledge HZWTECH for providing computational facilities.

The authors declare no conflict of interest.

[1] V. R. Palkar, D. C. Kundaliya, S. K. Malik, and S. Bhattacharya, Magnetoelectricity at room temperature in the $Bi_{0.9-x}Tb_xLa_{0.1}FeO_3$ system, Phys. Rev. B **69**, 212102 (2004).

[2] A. Glavic, C. Becher, J. Voigt, E. Schierle, E. Weschke, M. Fiebig, and T. Brueckel, Stability of spin-driven ferroelectricity in the thin-film limit: Coupling of magnetic and electric order in multiferroic $TbMnO_3$ films, Phys. Rev. B **88**, 054401 (2013).

[3] L. Ponet, S. Artyukhin, T. H. Kain, J. Wettstein, A. Pimenov, A. Shuvaev, X. Wang, S. W. Cheong, M. Mostovoy, and A. Pimenov, Topologically protected magnetoelectric switching in a multiferroic, Nature **607**, 81 (2022).

[4] D. Lebedev, J. T. Gish, E. S. Garvey, T. K. Stanev, J. Choi, L. Georgopoulos, T. W. Song, H. Y. Park, K. Watanabe, and T. Taniguchi, *et al.*, Electrical interrogation of thickness-dependent multiferroic phase transitions in the 2D antiferromagnetic semiconductor NiI_2, Adv. Funct. Mater. **33**, 2212568 (2023).

[5] S. Mishra, A. Roy, A. Sahoo, B. Satpati, A. Roychowdhury, P. K. Mohanty, C. K. Ghosh, and D. Bhattacharya, Room-temperature surface multiferroicity in Y_2NiMnO_6 nanorods, Phys. Rev. B **105**, 235429 (2022).

[6] K. Y. Dou, W. H. Du, Y. Dai, B. B. Huang, and Y. D. Ma, Two-dimensional magnetoelectric multiferroics in a $MnSTe/In_2Se_3$ heterobilayer with ferroelectrically controllable skyrmions, Phys. Rev. B **105**, 205427 (2022).

[7] E. Abreu, M. Savoini, L. Boie, P. Beaud, V. Esposito, M. Kubli, M. J. Neugebauer, M. Porer, U. Staub, and B. Burganov, *et al.*, Photoinduced structural dynamics of multiferroic $TbMnO_3$, Phys. Rev. B **106**, 214312 (2022).

[8] M. Y. Liu, T. L. Sun, T. T. Gao, Z. P. Bian, Z. L. Luo, X. Q. Liu, and X. M. Chen, Robust room-temperature ferroelectricity and magnetoelectric coupling effect in epitaxial $CaTiO_3/SmFeO_3$ thin films, J. Am. Ceram. Soc. **105**, 7558 (2022).

[9] H. X. Tan, M. L. Li, H. T. Liu, Z. R. Liu, Y. C. Li, and W. H. Duan, Two-dimensional ferromagnetic-ferroelectric multiferroics in violation of the d^0 rule, Phys. Rev. B **99**, 195434 (2019).

[10] H. M. Jang, J. H. Park, S. Ryu, and S. R. Shannigrahi, Magnetoelectric coupling susceptibility from magnetodielectric effect, Appl. Phys. Lett. **93**, 6694 (2008).

[11] R. Gupta, S. Chaudhary, and R. K. Kotnala, Interfacial charge induced magnetoelectric coupling at $BiFeO_3/BaTiO_3$ bilayer interface, ACS Appl. Mater. Interfaces **7**, 8472 (2015).

[12] Y. Q. Zhao, Z. S. Liu, G. Z. Nie, Z. H. Zhu, Y. F. Chai, J. N. Wang, M. Q. Cai, and S. l. Jiang, Structural, electronic, and charge transfer features for two kinds of MoS_2/Cs_2PbI_4 interfaces with optoelectronic applicability: Insights from first-principles, Appl. Phys. Lett. **118**, 173104 (2021).

[13] Y. Q. Zhao, Y. Xu, D. F. Zou, J. N. Wang, G. F. Xie, B. Liu, M. Q. Cai, and S. L. Jiang, First-principles study on photovoltaic properties of 2D Cs_2PbI_4-black phosphorus heterojunctions, J. Phys. Cendens. **32**, 195501 (2020).

[14] B. Sun, Y. F. Ding, P. B. He, Y. Q. Zhao, and M. Q. Cai, Tuning the band alignment and electronic properties of $GaSe/SnX_2$ ($X = S, Se$) two-dimensional van der Waals heterojunctions via an electric field, Phys. Rev. Appl. **16**, 044003 (2021).

[15] Z. L. Yu, C. Y. Zhang, Q. S. Tan, J. Y. Tao, X. X. Sun, L. Luo, F. Li, Y. Q. Zhao, C. Li, and L. Lang, First-principles study of phase transition in the α-In_2Se_3 /metal heterostructures, J. Phys. Cendens. **36**, 135502 (2024).

[16] G. T. Lin, H. L. Zhuang, X. Luo, B. J. Liu, F. C. Chen, J. Yan, Y. Sun, J. Zhou, W. J. Lu, and P. Tong, Tricritical

behavior of the two-dimensional intrinsically ferromagnetic semiconductor $CrGeTe_3$, Phys. Rev. B **95**, 245212 (2017).

[17] M. U. Rehman, Z. H. Qiao, and J. Wang, Valley-symmetry-broken magnetic topological responses in (Pt/Pd)(2)$HgSe_3$/$CrGeTe_3$ and Pd_2HgSe_3/CrI_3 through interfacial coupling, Phys. Rev. B **105**, 165417 (2022).

[18] S. Baidya, J. Yu, and C. H. Kim, Tunable magnetic topological insulating phases in monolayer CrI_3, Phys. Rev. B **98**, 155148 (2018).

[19] S. Bandyopadhyay, F. L. Buessen, R. Das, F. G. Utermohlen, N. Trivedi, A. Paramekanti, and I. Dasgupta, Exchange interactions and spin dynamics in the layered honeycomb ferromagnet CrI_3, Phys. Rev. B **105**, 184430 (2022).

[20] Y. J. Deng, Y. J. Yu, M. Z. Shi, Z. X. Guo, Z. H. Xu, J. Wang, X. H. Chen, and Y. B. Zhang, Quantum anomalous Hall effect in intrinsic magnetic topological insulator $MnBi_2Te_4$, Science **367**, 895 (2020).

[21] Y. X. Li, C. Liu, Y. C. Wang, Z. C. Lian, H. Li, Y. Wu, J. S. Zhang, and Y. Y. Wang, Giant nonlocal edge conduction in the axion insulator state of $MnBi_2Te_4$, Sci. Bull. **68**, 1252 (2023).

[22] J. Ding, D. F. Shao, M. Li, L. W. Wen, and E. Y. Tsymbal, Two-dimensional antiferroelectric tunnel junction, Phys. Rev. Lett. **126**, 057601 (2021).

[23] S. B. Fang, C. Yang, Q. H. Li, B. C. Wu, L. Q. Xu, S. Q. Liu, J. Yang, J. C. Ma, J. C. Dong, Y. Li, J. B. Yang, and J. Lu, Ferroelectric-tunable photoresponse in α-In_2Se_3 photovoltaic photodetectors: An *ab initio* quantum transport study, Phys. Rev. Appl. **19**, 024024 (2023).

[24] C. S. Liao, Y. F. Ding, Y. Q. Zhao, and M. Q. Cai, Band alignment engineering of a Ruddlesden-Popper perovskite-based heterostructure constructed using $Cs_2SnI_2Cl_2$ and α-In_2Se_3: The effects of ferroelectric polarization switching and electric fields, Appl. Phys. Lett. **119**, 182903 (2021).

[25] P. Jiang, L. L. Kang, H. Hao, X. H. Zheng, Z. Zeng, and S. Sanvito, Ferroelectric control of electron half-metallicity in A-type antiferromagnets and its application to non-volatile memory devices, Phys. Rev. B **102**, 245417 (2020).

[26] S. J. Wu, A. L. Li, Y. P. Wang, and F. P. Ouyang, Half-metallicity and Curie temperature enhancement of CrI_3 through boron atoms adsorption, Superlattices Microstruct. **159**, 107054 (2021).

[27] Y. Li, Z. Y. Jiang, J. H. Li, S. N. Xu, and W. H. Duan, Magnetic anisotropy of the two-dimensional ferromagnetic insulator $MnBi_2Te_4$, Phys. Rev. B **100**, 134438 (2019).

[28] M. Kan, S. Adhikari, and Q. Sun, Ferromagnetism in MnX_2 ($X = S, Se$) monolayers, Phys. Chem. Chem. Phys. **16**, 4990 (2014).

[29] D. J. O'Hara, T. C. Zhu, A. H. Trout, A. S. Ahmed, and R. K. Kawakami, Room temperature intrinsic ferromagnetism in epitaxial manganese selenide films in the monolayer limit, Nano Lett. **18**, 3125 (2018).

[30] J. S. Qian and S. P. Lau, $MnSe_2$ nanocubes as an anode material for sodium-ion batteries, Mater. Today Energy **10**, 62 (2018).

[31] X. T. Shang, S. Li, K. Wang, X. L. Teng, and S. D. Li, $MnSe_2$/Se composite nanobelts as an improved performance anode for lithium storage, Int. J. Electrochem. Soc. **14**, 6000 (2019).

[32] P. Manchanda, P. Kumar, and P. Dev, Defect-induced 4*p*-magnetism in layered platinum diselenide, Phys. Rev. B **103**, 144403 (2021).

[33] S. W. Deng, H. Hu, G. L. Zhuang, X. Zhong, and J. G. Wang, A strain-controlled C_2N monolayer membrane for gas separation in PEMFC application, Appl. Surf. Sci. **441**, 408 (2018).

[34] D. Xu, J. F. Zhang, Z. Y. Lu, and K. Liu, Magnetic and electronic transitions in monolayer electride Gd_2C induced by hydrogenation: A first-principles study, Phys. Rev. B **106**, 045138 (2022).

[35] X. L. Yan, P. Li, S. H. Wei, and B. Huang, Universal theory and basic rules of strain-dependent doping behaviors in semiconductors, Chin. Phys. Lett. **38**, 087103 (2021).

[36] M. P. K. Sahoo, J. Wang, Y. J. Zhang, T. Shimada, and T. Kitamura, Modulation of gas adsorption and magnetic properties of monolayer-MoS_2 by antisite defect and strain, J. Phys. Chem. C **120**, 14113 (2016).

[37] A. Bafekry, S. Farjami Shayesteh, M. Ghergherehchi, and F. M. Peeters, Tuning the bandgap and introducing magnetism into monolayer BC_3 by strain/defect engineering and adatom/molecule adsorption, J. Appl. Phys. **126**, 144304 (2019).

[38] L. T. Romano, C. G. Van De Walle, B. S. Krusor, R. Lau, and R. S. Kern, Effect of Si doping on the strain and defect structure of GaN thin films, Phys. B Condens. Matter **273**, 50 (1999).

[39] C. J. Cui, F. Xue, W. J. Hu, and L. J. Li, Two-dimensional materials with piezoelectric and ferroelectric functionalities, NPJ 2D Mater. Appl. **2**, 18 (2018).

[40] T. Kimura, T. Goto, H. Shintani, K. Ishizaka, T. Arima, and Y. Tokura, Magnetic control of ferroelectric polarization, Nature **426**, 55 (2003).

[41] C. S. Liao, Y. F. Ding, Y. Q. Zhao, and M. Q. Cai, Band alignment engineering of a Ruddlesden-Popper perovskite-based heterostructure constructed using $Cs_2SnI_2Cl_2$ and α-In_2Se_3: The effects of ferroelectric polarization switching and electric fields, Appl. Phys. Lett. **119**, 182903 (2021).

[42] Y. K. Zhang, Q. Yang, L. L. Tao, E. Y. Tsymbal, and V. Alexandrov, Effects of strain and film thickness on the stability of the rhombohedral phase of HfO_2, Phys. Rev. Appl. **14**, 014068 (2020).

[43] Z. J. Chen, Q. Yang, L. L. Tao, and E. Y. Tsymbal, Reversal of the magnetoelectric effect at a ferromagnetic metal/ferroelectric interface induced by metal oxidation, NPJ Comput. Mater. **7**, 204 (2021).

[44] Z. L. Yu, J. Y. Tao, L. Lin, X. X. Sun, Z. J. Zou, L. Fen, Y. Q. Zhao, L. Biao, L. Chang, and G. H. Liao, Electronic structure characteristics of two-dimensional ferroelectric heterostructures α-In_2Se_3/ZnSe, J. Phys. Cendens. **35**, 055703 (2023).

[45] L. L. Kang, X. H. Zheng, P. Jiang, Z. Z. Feng, and G. F. Zhao, Tuning magnetism by electric field in $MnPS_3/Sc_2CO_2$ van der Waals heterostructure, Appl. Phys. Lett. **122**, 082902 (2023).

[46] Y. F. Lang, D. F. Zou, Y. Xu, S. L. Jiang, Y. Q. Zhao, and Y. S. Ang, Electronic characteristics of the two-dimensional van der Waals ferroelectric α-$In_2Se_3/Cs_3Bi_2I_9$ heterostructures, Appl. Phys. Lett. **124**, 052903 (2024).

[47] Z. Liu, L. J. Deng, and B. Peng, Ferromagnetic and ferroelectric two-dimensional materials for memory application, Nano Res. **14**, 1802 (2021).
[48] H. Y. Lyu, Z. Zhang, J. Y. You, Q. B. Yan, and G. Su, Two-dimensional intercalating multiferroics with strong magnetoelectric coupling, J. Phys. Chem. Lett. **13**, 11405 (2022).
[49] L. Hu, L. Cao, L. W. Li, J. M. Duan, X. Q. Liao, F. C. Long, J. Zhou, Y. G. Xiao, Y. J. Zeng, and S. Q. Zhou, Two-dimensional magneto-photoconductivity in non-van der Waals manganese selenide, Mater. Horizons **8**, 1286 (2021).
[50] P. E. Blöchl, Projector augmented-wave method, Phys. Rev. B **50**, 17953 (1994).
[51] G. Kresse and J. Furthmüller, Efficient iterative schemes for ab initio total-energy calculations using a plane-wave basis set, Phys. Rev. B **54**, 11169 (1996).
[52] G. Kresse and D. Joubert, From ultrasoft pseudopotentials to the projector augmented-wave method, Phys. Rev. B **59**, 1758 (1999).
[53] S. Grimme, J. Antony, S. Ehrlich, and H. Krieg, A consistent and accurate ab initio parametrization of density functional dispersion correction (DFT-D) for the 94 elements H-Pu, J. Chem. Phys. **132**, 154104 (2010).
[54] J. Taylor, H. Guo, and J. Wang, Ab initio modeling of quantum transport properties of molecular electronic devices, Phys. Rev. B **63**, 245407 (2001).
[55] W. Q. Xie, Z. W. Lu, C. C. He, X. B. Yang, and Y. J. Zhao, Theoretical study of tunable magnetism of two-dimensional $MnSe_2$ through strain, charge, and defect, J. Phys. Condens. Matter **33**, 215803 (2021).
[56] S. Grimme, Semiempirical GGA-type density functional constructed with a long-range dispersion correction, J. Comput. Chem. **27**, 1787 (2006).
[57] J. P. Perdew, K. Burke, and M. Ernzerhof, Generalized gradient approximation made simple, Phys. Rev. Lett. **77**, 3865 (1996).
[58] J. Maassen, M. Harb, V. Michaud-Rioux, Y. Zhu, and H. Guo, Quantum transport modeling from first principles, Proc. IEEE Inst. Electr. Electron. Eng. **101**, 518 (2012).
[59] Y. Meir and N. S. Wingreen, Landauer formula for the current through an interacting electron region, Phys. Rev. Lett. **68**, 2512 (1992).
[60] See Supplemental Material at http://link.aps.org/supplemental/10.1103/PhysRevApplied.21.064012 for the detailed data. These data contain the detailed geometrical structure, biaxial train controlled Heisenberg model parameters, projected density of states of $MnSe_2/In_2Se_3$ heterostructure.
[61] H. M. Hu and G. Ouyang, Interface-induced transition from Schottky-to-Ohmic contact in Sc_2Co_2-based multiferroic heterojunctions, Phys. Chem. Chem. Phys. **23**, 827 (2021).
[62] K. Cao, G. C. Guo, D. Vanderbilt, and L. X. He, First-principles modeling of multiferroic RMn_2O_5, Phys. Rev. Lett. **103**, 257201 (2009).
[63] M. Azmoonfar, M. R. Roknabadi, M. Modarresi, and A. Mogulkoc, Characterization of two dimensional ferromagnetic binary and Janus manganese dichalcogenides, J. Magn. and Magn. Mater. **556**, 169412 (2022).
[64] J. M. D. Coey, M. Venkatesan, and C. B. Fitzgerald, Donor impurity band exchange in dilute ferromagnetic oxides, Nat. Mater. **4**, 173 (2005).
[65] H. X. Deng, J. B. Li, S. S. Li, J. B. Xia, A. Walsh, and S. H. Wei, Origin of antiferromagnetism in CoO: A density functional theory study, Appl. Phys. Lett. **96**, 162508 (2010).
[66] A. Walsh, J. L. F. Da Silva, and S. H. Wei, Theoretical description of carrier mediated magnetism in cobalt doped ZnO, Phys. Rev. Lett. **100**, 256401 (2008).
[67] J. B. Goodenough, Theory of the role of covalence in the perovskite-type manganites [La, M(II)]MnO_3, Phys. Rev. **100**, 564 (1955).
[68] J. B. Goodenough, An interpretation of the magnetic properties of the perovskite-type mixed crystals $La_{1-x}Sr_xCoO_{3-\lambda}$, J. Phys. Chem. Solids **6**, 287 (1958).
[69] J. Hong, C. J. Kang, and J. Kim, Role of electronic correlations in room-temperature ferromagnetism of monolayer $MnSe_2$, Phys. Rev. B **106**, 195428 (2022).
[70] Z. W. Zhang, Z. S. Liu, J. J. Zhang, B. N. Sun, D. F. Zou, G. Z. Nie, M. Y. Chen, Y. Q. Zhao, and S. L. Jiang, Interfacial contact barrier and charge carrier transport of MoS_2 /metal(001) heterostructures, Phys. Chem. Chem. Phys. **25**, 9548 (2023).